

Cite this: *Nanoscale*, 2021, **13**, 20034

## Resistance of single domain walls in half-metallic CrO<sub>2</sub> epitaxial nanostructures

Lijuan Qian, Shiyu Zhou, Kang Wang and Gang Xiao \*

Magnetic domain structures are active electron transport agents and can be used to induce large magnetoresistance (MR), particularly in half-metallic solids. We have studied the excess resistance induced by a single magnetic domain wall in a one-dimensional half-metallic CrO<sub>2</sub> nanoscale conductor with a built-in constriction whose channel width ( $d$ ) ranges from 30 to 200 nm. We observed that the domain wall-induced MR is enhanced by 70 fold when  $d$  decreases from 200 nm to 30 nm. We speculate that the enhancement is due to the increased domain wall resistance (DWR) and the extra contribution of ballistic magnetoresistance (BMR). We have uncovered a large size effect of  $d$  on the MR induced by the domain wall, which scales with  $d$  as  $d^{-1.87 \pm 0.32}$ . Accordingly, we predict that the MR ratio of a simple CrO<sub>2</sub> nanowire impregnated with a constriction at a 150 nm<sup>2</sup> cross-section could reach 100%. This large MR far exceeds that of a conventional ferromagnetic nanowire, confirming the role of half metallicity on enhanced magneto-transport.

Received 24th August 2021,  
Accepted 9th November 2021

DOI: 10.1039/d1nr05555k

rsc.li/nanoscale

### Introduction

It is known that spin textures such as domain walls (DWs) can induce excess resistivity in ferromagnetic materials.<sup>1–6</sup> According to the Levy-Zhang model, the excess resistivity originates from the mixing of two spin current channels within non-homogeneous spin states.<sup>1</sup> Research on domain-wall resistance (DWR) and electron transport in spin textures benefits their potential application in spintronic devices.<sup>7,8</sup> Half-metallic ferromagnets with 100% spin polarization are ideal systems to investigate DWR, as their infinitely large spin asymmetry manifests prominently in magneto-transport. Among them, half metal CrO<sub>2</sub> has been extensively studied, and its half metallicity has been confirmed through various experimental techniques.<sup>9–12</sup> Previously, we have reported for the first time the observation of the excess resistance induced by a single DW in CrO<sub>2</sub>.<sup>13</sup> We estimated through magneto-transport measurements and micromagnetic simulations that the DW resistivity ratio ( $\Delta\rho_{\text{DW}}/\rho_0$ ) in CrO<sub>2</sub> is in the range of 1.3% to 13.2% at the temperature of 5 K.  $\Delta\rho_{\text{DW}}$  is the excess resistivity induced by a single DW and  $\rho_0$  is the resistivity of the CrO<sub>2</sub> in the single-domain state.<sup>13</sup> Afterwards, we investigated the resistivity induced by general spin textures besides DWs. We uncovered the correlation between the magnetoresistance (MR) and spin curvature in CrO<sub>2</sub>. The spin curvature is defined as the spatial nonuniformity of spins.<sup>2</sup> From the empirical cor-

relation between the excess resistivity and spin curvature of spin textures, we estimated the DWR in CrO<sub>2</sub>. The DWR predicted from the empirical relationship is consistent with our previous measurement results, which shows that the DWR and spin curvature induced MR have the same physical origin.<sup>2,13</sup> Both can be explained by the Levy-Zhang model and the magnitude of the excess resistivity of a spin texture is determined by its spin configuration and the spin asymmetry parameter  $\left(\frac{\rho_{\uparrow}}{\rho_{\downarrow}}\right)$  of the material. These studies provide guidance for us to manipulate the DW configuration and achieve a large DWR by modifying CrO<sub>2</sub> nanostructures, which is of great interest to both fundamental research and spintronic applications.

In this work, we investigated the DWR in CrO<sub>2</sub> epitaxial nanostructures with varying structural sizes and explored the size effects on the DW configuration and the corresponding DWR. This work distinguishes from previous works in that it explores the electron transport in DWs from a diffusive regime to a quasi-ballistic regime. The single DWs were created and annihilated in nanostructures with an asymmetrical weak link, which we call *nano-constriction* where the constriction width  $d$  varies from 30 to 200 nm. The DWR is substantially enhanced when the constriction width  $d$  reduces, which is possibly because the electrons cannot accommodate the spin changes inside the nano-constrictions when the constriction size is decreased to tens of nanometers. The DWR scales with  $S^{-1.87 \pm 0.32}$ , where  $S$  is the cross-sectional area of the constriction. Based on this power law, a large MR of 100% is expected

Department of Physics, Brown University, Providence, Rhode Island 02912, USA.  
E-mail: Gang\_Xiao@Brown.edu

when  $S$  is reduced to 150 nm<sup>2</sup>, e.g., in a 10 nm-thick and 15 nm-wide constriction. The DMR value of CrO<sub>2</sub> is much larger than those of other non-half-metallic magnetic solids such as Ni and NiFe at comparable cross-sectional areas.<sup>14</sup>

## Experimental

We prepared epitaxial CrO<sub>2</sub> nanostructures using the techniques of electron-beam lithography, chemical vapor deposition (CVD), and selective area growth (SAG) without post-deposition patterning. The CrO<sub>2</sub> nanostructures are grown on TiO<sub>2</sub> single crystal substrates. A detailed preparation process can be found in our previous studies.<sup>2,9,13</sup> Our earlier experiments have shown that the CrO<sub>2</sub> thin films deposited this way exhibit a spin polarization of 0.96 ± 0.01 at 1.85 K.<sup>9</sup> In this work, we studied a nanowire with a built-in weak link which we call a nano-constriction with a variable constriction width. We were able to generate or annihilate a single DW located near the constriction. We then studied the DW configuration and DWR through the complementary micromagnetic simulations and magneto-transport measurements.

Micromagnetic simulation is an effective method to reveal magnetization states in magnetic nanostructures. For every structure studied in this work, we performed a micromagnetic simulation using mumax<sup>3</sup>, a GPU-accelerated program developed at Ghent University.<sup>15</sup> The software simulates the time and spatial evolution of spin configurations based on the Landau-Lifshitz micromagnetic formalism using the method of finite difference discretization. We obtained the equilibrium magnetization states in the CrO<sub>2</sub> nanostructures under various external magnetic fields by minimizing the total free energy including four energy terms.

The Zeeman energy originates from the interaction between the magnetization and external field. The energy density is expressed as  $\epsilon_{\text{Zeeman}} = -\vec{M} \cdot \vec{B}_{\text{ext}}$ , where  $\vec{M} = M_s \hat{m}$  is the magnetization vector,  $M_s = 640 \text{ emu cm}^{-3}$  is the saturation magnetization experimentally obtained at 10 K,<sup>16</sup>  $\hat{m}$  is the unit magnetization vector, and  $\vec{B}_{\text{ext}}$  is the external magnetic field.

The exchange energy arises from the exchange coupling between neighboring spins, which is responsible for the ferromagnetic ordering. The energy density is  $\epsilon_{\text{exchange}} = -\frac{1}{2} \vec{M} \cdot \vec{B}_{\text{exch}}$ , where  $\vec{B}_{\text{exch}} = 2 \frac{A_{\text{ex}}}{M_s} \cdot \hat{m}$  is the effective field due to the Heisenberg exchange interaction, and  $A_{\text{ex}}$  is the exchange constant. Based on the Curie temperature ( $T_C = 398 \text{ K}$ ) of CrO<sub>2</sub>, the exchange constant  $A_{\text{ex}}$  is estimated to be  $4.6 \times 10^{-7} \text{ erg cm}^{-1}$ .<sup>16</sup>

The demagnetization energy,  $\epsilon_{\text{demag}} = -\frac{1}{2} \vec{M} \cdot \vec{B}_{\text{demag}}$ , accounts for the shape anisotropy, where  $\vec{B}_{\text{demag}}$  is the demagnetization field. Finally, the magnetocrystalline anisotropy energy is determined by the crystal structure of the material. In 100 nm-thick CrO<sub>2</sub> epitaxial films, the uniaxial anisotropy axis is along the [001] direction.<sup>16</sup> The corresponding energy density is  $\epsilon_{\text{anis}} = -\frac{1}{2} \vec{M} \cdot \vec{B}_{\text{anis}}$ , where  $\vec{B}_{\text{anis}} = \frac{2K_{u1}}{M_{\text{sat}}} (\hat{u} \cdot \hat{m}) \hat{u}$  is the

**Table 1** Physical parameters used in micromagnetic simulations

Parameter	Value	Ref.
Saturation magnetization $M_s$	640 emu cm <sup>-3</sup>	16
Exchange constant $A_{\text{ex}}$	$4.6 \times 10^{-7} \text{ erg cm}^{-1}$	16
Uniaxial anisotropy constant $K_{u1}$	$9.2 \times 10^4 \text{ erg cm}^{-3}$	16
Cell size	4 nm	N/A
Gilbert damping coefficient $\alpha$	0.023	18

effective anisotropy field,  $\hat{u}$  is the unit vector denoting the uniaxial anisotropy axis, and  $K_{u1}$  is the uniaxial anisotropy constant which has been previously measured as  $9.2 \times 10^4 \text{ erg cm}^{-3}$ .<sup>16</sup> Table 1 summarizes the parameters adopted in our simulations. The magnetic films are discretized into cells with a cell size of 4 nm which is smaller than the Bloch wall width  $\sqrt{\frac{A_{\text{ex}}}{K_{u1}}} = 22 \text{ nm}$  and the exchange length  $\sqrt{\frac{A_{\text{ex}}}{K_d}} = \sqrt{\frac{A_{\text{ex}}}{2\pi M_s^2}} = 4.2 \text{ nm}$ <sup>17</sup> to ensure simulation accuracy.

## Results and discussion

Fig. 1(a) shows the schematic diagram of the nanostructure with an asymmetrical weak link. The longitudinal axis of the structure, denoted as the  $x$  axis, is along the [001] direction, which is the magnetocrystalline easy axis in the 100 nm-thick CrO<sub>2</sub> epitaxial films.<sup>16</sup> The transverse axis of the structure, denoted as the  $y$  axis, is along the [010] direction, which is the hard axis. The width of the main lead of the structure is one micron, while the constriction width,  $d$ , varies ( $d = 30, 50, 120$ , and 200 nm). The boundaries on the left and right sides of the constriction form wedges with angles of 60° and 15°, respectively, relative to the  $x$  axis. The asymmetry is essential to introducing the DW state in the vicinity of the constriction through the external magnetic field. Moreover, varying the constriction width is essential for modifying the DW configuration near the constriction where the demagnetization energy plays an important role in determining the magnetization state.

Due to the shape anisotropy, the magnetic field required to reverse magnetization, which we denote as the reversing field ( $B_{\text{rev}}$ ), is different for spins on the left and right sides of the constrictions. In our design,  $|B_{\text{rev}}(\text{left})| < |B_{\text{rev}}(\text{right})|$ . When the applied field ( $B_{\text{app}}$ ) is in between the two reversing fields, i.e.,  $|B_{\text{rev}}(\text{left})| < |B_{\text{app}}| < |B_{\text{rev}}(\text{right})|$ , the magnetization on the left is along the opposite direction to the magnetization on the right side of the constriction. Therefore, a DW is formed near the constriction. Far away from the constriction, four leads are designed for the 4-probe measurement of the resistivity of the nanostructures. Fig. 1(b) is a representative scanning electron microscopy (SEM) image of the nanostructure with  $d = 50 \text{ nm}$ , with the dark region as the epitaxial CrO<sub>2</sub> nanostructure and the light region as SiO<sub>2</sub>. From the SEM image, we analyze the roughness of the edges of the nanostructure and conclude that the uncertainty in the constriction width  $d$  is about 12 nm.

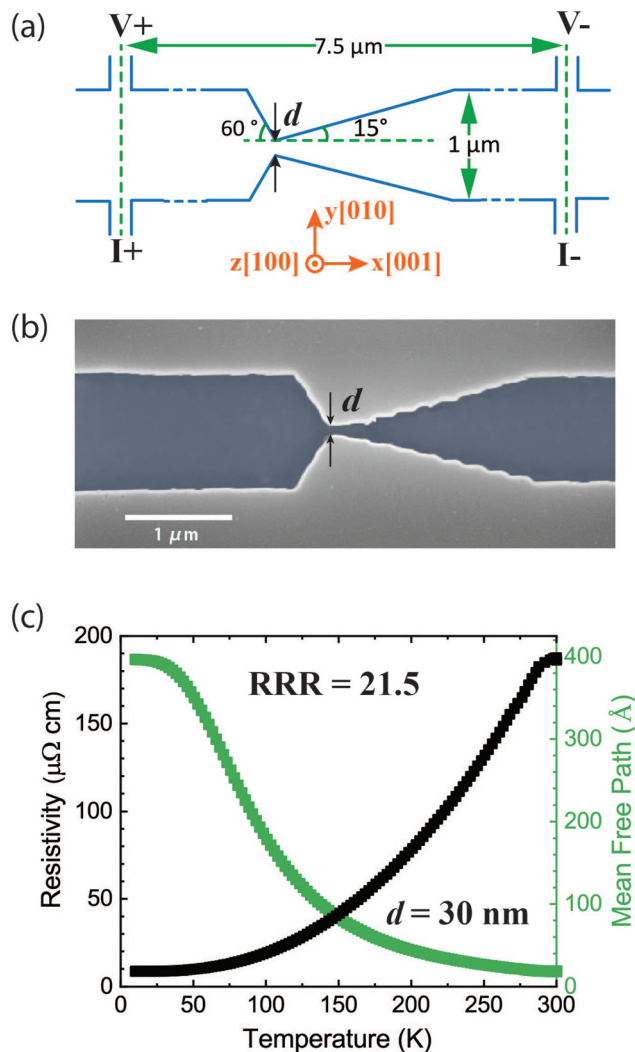


**Fig. 1** (a) Schematic of a 100 nm-thick CrO<sub>2</sub> nanostructure with a constriction (neck) width  $d$  for magneto-transport measurement. The longitudinal axis of the wire is along the magnetocrystalline easy axis ( $x$  axis). (b) Scanning electron micrograph of an epitaxial CrO<sub>2</sub> nanostructure with  $d = 50$  nm, where the dark region is CrO<sub>2</sub> and the light region is SiO<sub>2</sub>. (c) Temperature dependence of resistivity (black curve) and the estimated electron mean free path (green curve) of an epitaxial CrO<sub>2</sub> nanostructure as shown in (a) with  $d = 30$  nm. The residual resistivity ratio (RRR),  $\frac{\rho_{300\text{K}}}{\rho_{10\text{K}}}$ , is 21.5.

Fig. 1(c) shows the temperature dependence of the resistivity of the CrO<sub>2</sub> nanostructure with  $d = 30$  nm in the temperature range of 10 to 300 K. We convert the resistance data to resistivity in the nanostructure using the general-purpose simulation software COMSOL Multiphysics®. We observe that the resistivity decreases from 186.0  $\mu\Omega$  cm at room temperature to 8.7  $\mu\Omega$  cm at 10 K, yielding a large residue resistivity ratio  $\text{RRR} = \frac{\rho_{300\text{K}}}{\rho_{10\text{K}}}$  of 21.5 which indicates a high crystalline quality of the nanostructure. As references, the RRR of a single crystal bulk CrO<sub>2</sub> is about 50,<sup>19</sup> and the RRR of the high-quality epitaxial CrO<sub>2</sub> nanostructures is typically in the range of 20 to 30.<sup>2,13,20</sup> Based on the Boltzmann theory,<sup>19</sup> we estimate

the electron mean free path (MFP) at each temperature according to

$$l(T) \cong \frac{(2\pi)^3 \hbar}{e^2} \frac{1}{A_{\text{FS}}^{\uparrow} + A_{\text{FS}}^{\downarrow}} \frac{3}{\rho(T)} \quad (1)$$

where  $A_{\text{FS}}^{\uparrow}$  and  $A_{\text{FS}}^{\downarrow}$  are Fermi surface areas of the majority and minority spins, respectively,  $\rho(T)$  is the resistivity at temperature  $T$ ,  $\hbar$  is the reduced Planck constant, and  $e$  is the elementary charge. Spin flip scattering is not considered in the estimation. According to the band structure calculations of CrO<sub>2</sub>,  $A_{\text{FS}}^{\uparrow} = 8.86 \text{ \AA}^{-2}$  and  $A_{\text{FS}}^{\downarrow} = 0.19$ . The calculated mean free path  $l(T)$  is plotted in Fig. 1(c) in green and scaled against the right axis. The MFP increases from 18  $\text{Å}$  at 300 K to 397  $\text{Å}$  at 10 K. At 10 K, the MFP exceeds the constriction width  $d = 30$  nm, and the electron transport becomes ballistic or at least quasi-ballistic. Note that in previous studies, device sizes were larger than the electron MFP and the electron transport was dissipative.<sup>2,13</sup> The MR behavior of spin textures in the half-metallic CrO<sub>2</sub> at the quantum transport regime is elusive and remains to be explored.

Fig. 2(a) and (b) show the micromagnetic simulation results of the spin maps with domain walls created in the presence of appropriate reversing fields around constrictions with  $d = 30, 50, 120,$  and  $200$  nm, respectively. Away from a constriction, the nanostructure consists of two single domains (right versus left side) with spins along either the  $+x$  or  $-x$  direction, respectively. Near each constriction, a DW complex is formed with varying details from one constriction to another, as represented by the color rendering and the color wheel ( $x$ - $y$  plane). The white ( $m_z = +1$ ) and black ( $m_z = -1$ ) regions rep-

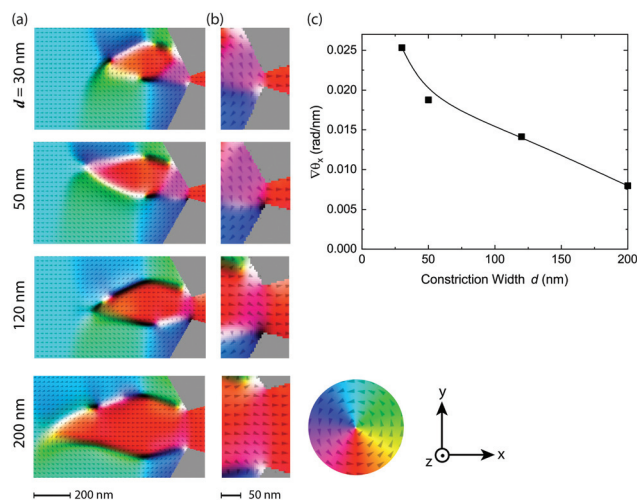


**Fig. 2** (a) Micromagnetic simulation results of magnetic domain wall (DW) configurations in CrO<sub>2</sub> nanostructures with  $d = 30, 50, 120,$  and  $200$  nm, respectively. (b) Enlarged spin maps around the constrictions. The colors represent the magnetization direction. The  $x$ - $y$  plane magnetization direction color map is shown in the color wheel. The brightness represents the out-of-plane magnetization contribution, where white and black correspond to the upward ( $+z$ ) and downward ( $-z$ ) magnetization, respectively. (c) The spatial gradient of spins along the  $x$  axis at the constriction,  $\nabla\theta_x$ , in nanostructures with different constriction widths  $d$ .

represent the out-of-plane spins. Fig. 2(a) shows that the DWs are located on the left side of the constriction so that the demagnetization field due to the DW is minimized. Spins inside the DWs rotate out-of-plane. Such DWs are known as Bloch walls which tend to form when a film is thick. The contour of the DW is approximately a semioval. From Fig. 2(a), we observe that as the constriction width  $d$  gets smaller, the semioval DW contracts to be closer, or more localized, to the constriction, and moreover, the spin curvature in the constriction gets larger. Fig. 2(b) shows the magnified spin maps near the constrictions. At the smallest  $d = 30$  nm, spins rotate by about  $90^\circ$  across the constriction, where spins on the left of the constriction align mostly along the  $y$  axis while spins on the right side of the constriction align along the  $x$  axis. In contrast, at the largest  $d = 200$  nm, spins are mostly aligned along the  $+x$  direction across the constriction with little change in the spin curvature. Fig. 2(c) shows the spatial gradient of spins along the  $x$  axis, *i.e.*, the spin curvature  $\nabla\theta_x$ , in the constriction, versus the constriction width  $d$ , where  $\theta$  is the angle from the  $x$ -axis in the  $x$ - $y$  plane. From  $d = 200$  to  $30$  nm, the spin curvature at the center of the constriction increases from  $0.008$  nm $^{-1}$  to  $0.025$  nm $^{-1}$ . This indicates that the DW configuration is very sensitive to the constriction size. The tinier the constriction is, the larger the spin curvature appears. Note that the spin curvature around the constrictions as shown in Fig. 2(b) has a major implication on the magneto-transport as the narrowest region contributes most to the resistance.

We generated and annihilated DWs in the nanostructures by applying moderate reversing magnetic fields. Fig. 3(a)–(d) show the field dependent resistance change relative to the zero-field resistance,  $\Delta R = R(B) - R(0)$ , and the corresponding magnetoresistance  $MR = \frac{R(B) - R(0)}{R(0)}$ , at  $d = 30, 50, 120,$  and  $200$  nm, respectively.

The continuous change in MR with the magnetic field is primarily due to the spin curvature change in the angled region. When the external field is parallel (anti-parallel) to the magnetization, MR decreases (increases) with the increasing magnetic field because the spin curvature is suppressed (enhanced) by the magnetic field. This behavior has been studied quantitatively in our previous work.<sup>2</sup> It is independent of the domain wall creation and annihilation process. The abrupt jump in resistance  $\Delta R_{B'-A'}$  is specifically related to the creation of a domain wall. Using Fig. 3(a), in which  $d = 30$  nm, as an example, we specify the magnetization reversal and corresponding MR hysteresis loop as follows. Initiating at  $-500$  Oe, the whole nanostructure has its magnetization along the  $-x$  direction. We started measuring the resistance from  $-500$  to  $0$  Oe, reaching point A. Reversing the field to the  $+x$  direction and increasing the field to  $110$  Oe (point A'), the overall spin curvature of the nanostructure increases for lowering the Zeeman energy and, the resistance increases continuously with the external field. When the magnetic field increases to  $136$  Oe (point B'), magnetization on the left side of the constriction reverses, creating a DW as shown in Fig. 2(a). When the magnetic field continues to increase to  $156$  Oe (point C'), the magnetization on the right side of the con-

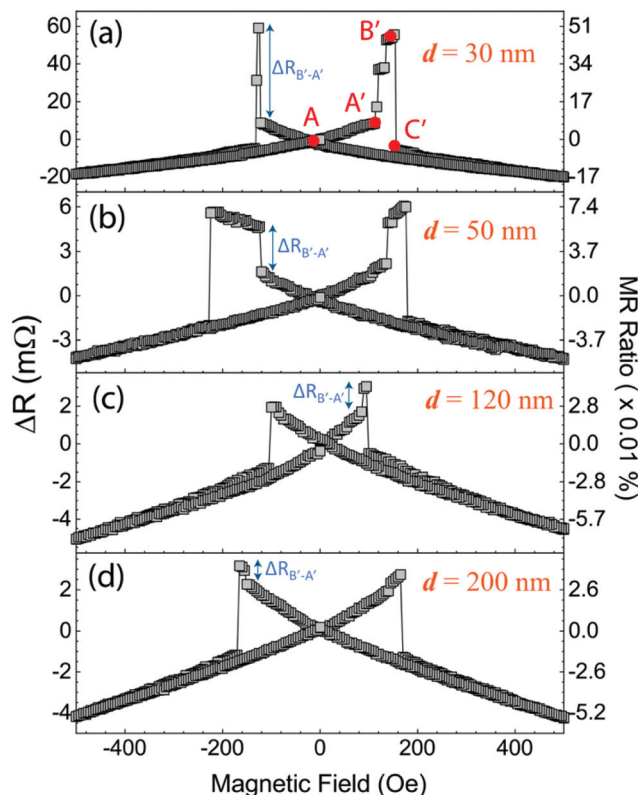


**Fig. 3** (a–d) Magnetic field induced resistance change and magnetoresistance (MR) relative to zero-field resistance in CrO<sub>2</sub> nanostructures with  $d = 30, 50, 120,$  and  $200$  nm, respectively, at  $T = 10$  K. When the external magnetic field increases, the resistance increases abruptly (from point A' to point B') due to the creation of a domain wall (DW). The corresponding resistance change upon domain wall generation is denoted as  $\Delta R_{B'-A'}$ .

striction is reversed to the  $+x$  direction. The DW is annihilated, and the resistance drops precipitously. As the magnetic field further increases to  $+500$  Oe, the resistance decreases continuously with the increasing field due to the decrease of the spin curvature. We denote the abrupt increase in resistance due to the appearance of a DW (from point A' to point B') as  $\Delta R_{B'-A'}$ . There seem to be some intermediate states between A' and B' at  $d = 30$  nm, which has not been observed in other nanostructures. We speculate that when  $d = 30$  nm, the MR is highly sensitive to the DW configuration and a slight change in the spin state manifests itself in the MR. Fig. 3(b)–(d) show similar magneto-transport behaviors, indicating the existence of the process of DW creation and annihilation as in Fig. 3(a), for constrictions of  $d = 50, 120,$  and  $200$  nm, respectively.

To estimate the DWR at zero field, we performed the “half-hysteresis loop” measurement as shown in Fig. 4. Similar to the full loop measurement, we started the measurement from  $+500$  Oe, where the magnetization in the wire was initialized along the  $+x$  direction, and then the field was decreased to zero reaching point A. From  $0$  Oe (point A) to  $-138$  Oe (point A'), an external field antiparallel to the sample's magnetization was applied. When the external field increased to  $-140$  Oe

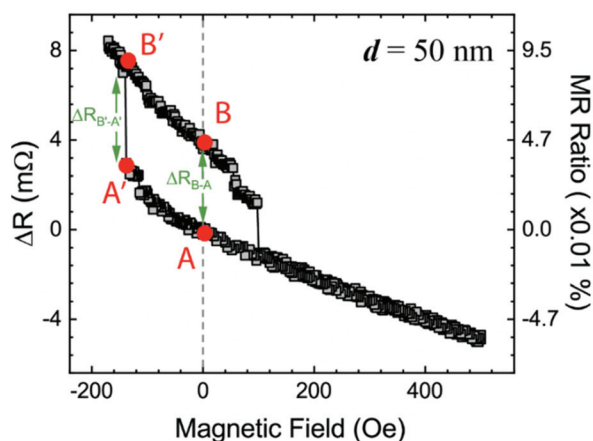


Fig. 4 Magnetic field induced resistance change and magnetoresistance (MR) relative to zero-field resistance in  $\text{CrO}_2$  nanostructures with  $d = 50$  nm at  $T = 10$  K. Point A represents the resistance without the domain wall (DW) at zero field. Point A' represents the resistance without the DW at a  $-140$  Oe field. Point B' is the state with the DW at  $-140$  Oe. Point B is the state with the DW at zero field.  $\Delta R_{B-A}$  is the zero-field DWR.  $\Delta R_{B'-A'}$  is the DWR at a  $-140$  Oe field, which is the same as the  $\Delta R_{B'-A'}$  denoted in Fig. 5.

(point B'), the DW was created. Instead of further increasing the magnetic field to wipe out the DW as in Fig. 3, we slowly decreased the magnetic field back to zero field (point B). The resistance change at zero field is  $\Delta R_{B-A}$ . In our previous study, we have analyzed that the contributions from other MR effects apart from the DWR to the resistance change at zero fields are negligible.<sup>13</sup> Therefore,  $\Delta R_{B-A}$  can be considered as the resistance change induced by the creation of a magnetic DW. However, this type of measurement is not easy to implement when  $d$  is large because the DW exists in a narrow range of the magnetic field. Fortunately, we notice that in Fig. 4, the resistance change from point A' to point B' is close to that from point A to point B. As mentioned before, the resistance changes from A to A' and from B to B' are due to the change of the spin curvature in response to the external field. In the asymmetrical weak link design, as shown in Fig. 1(a), the spin curvature change arises mostly from the non-uniform region with angled wedges. Consequently, the spin curvature-induced MR is dominated by spins on the right side of the constriction because the right side of the constriction contributes most to the measured resistance due to the small width and large length. The spin curvature variation in this region is similar from A to A' and B to B' because the creation or annihilation of the DW has little effect on the magnetization on the right side of the constriction as shown in Fig. 2(a). As a result,  $\Delta R_{B'-A'} \approx \Delta R_{B-A}$ , and  $\Delta R_{B'-A'}$  is therefore a good measure of the DWR.

We obtained  $\Delta R_{B'-A'}$  in all nanostructures with different constriction widths  $d$  shown in Fig. 3(a)–(d). For each sample,  $\Delta R_{B'-A'}$  was derived from the average of multiple measurements. From  $d = 200$  to  $30$  nm,  $\Delta R_{B'-A'}$  increases from  $0.6$  mΩ to  $42$  mΩ by  $70$  fold. The corresponding MR =  $\frac{\Delta R_{B'-A'}}{R_0}$  increases from  $0.0075\%$  to  $0.36\%$  by  $48$  fold. In Fig. 5, we plot

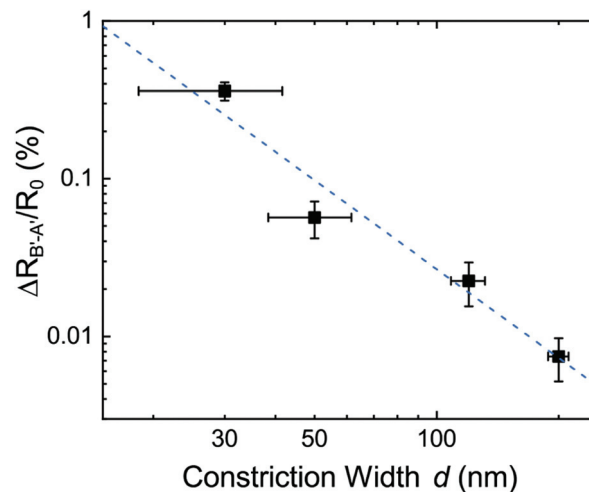


Fig. 5  $\frac{\Delta R_{B'-A'}}{R_0}$  versus constriction width  $d$ , plotted on a log–log scale. The dashed line is a power fit to the experimental results.

the DWR ratio,  $\frac{\Delta R_{B'-A'}}{R_0}$ , versus the constriction width  $d$ , on a log–log scale. The horizontal error bars represent the uncertainties in constriction widths as estimated from the SEM images. The vertical error bars were derived from the standard deviation of multiple measurements. The dashed line indicates fitting to the data with  $\frac{\Delta R_{B'-A'}}{R_0}$  proportional to  $d^{-1.87 \pm 0.32}$ . This result indicates that the DMR of our nanostructures is highly sensitive to the dimensions of the constriction. The DWR is dramatically enhanced through reducing the constriction size.

Levy and Zhang's study calculates the DWR originating from the spin mixing of two spin current channels inside the DW in the diffusive transport regime. When the current flows perpendicular to the DW, the corresponding DWR is estimated to be

$$R_{\text{CPW}} = \frac{\xi^2}{5} \frac{(\rho_0^\uparrow - \rho_0^\downarrow)^2}{\rho_0^\uparrow \rho_0^\downarrow} \left( 3 + \frac{10\sqrt{\rho_0^\uparrow \rho_0^\downarrow}}{\rho_0^\uparrow + \rho_0^\downarrow} \right), \quad (2)$$

where  $\rho_0^\uparrow$  and  $\rho_0^\downarrow$  are resistivities for the spin up and spin down states, respectively, and  $\xi \equiv \frac{\pi \hbar^2 k_F}{4m\lambda J}$  in which  $J$  denotes the exchange splitting,  $m$  is the electron mass, and  $\lambda$  is the DW width.

In contrast, in a highly constricted nanostructure, when the spin flip MFP is much larger than the DW width such that the electrons cannot accommodate the spin change across the constriction adiabatically, the ballistic MR (BMR) effect occurs. The magnitude of BMR is approximately

$$\frac{\Delta R}{R} (\%) = \frac{2P^2}{1-P^2} F(P, \lambda) \quad (3)$$

where  $P$  is the spin polarization at the Fermi level and  $F(P, \lambda)$  is the function showing the accommodation of spins inside the

DW.<sup>21–25</sup> When the DW width  $\lambda$  is comparable with the Fermi wavelength  $\lambda_F$ ,  $F(P, \lambda)$  behaves as  $\exp(-\beta\lambda)$ . When  $\lambda \gg \lambda_F$ , which is the case in our study,  $F(P, \lambda)$  behaves as  $\frac{1}{\alpha\lambda^2}$ ,<sup>21–23,25</sup> where  $\beta$  and  $\alpha$  are constants.

In both eqn (2) and (3), the domain wall width  $\lambda$  indeed characterizes the spin curvature inside the domain walls because a standard DW configuration is adopted in calculations. In this study, due to the complexity of the domain wall induced around the constriction, the spin curvature is not characterized by the domain wall width  $\lambda$ . Instead it is determined by the constriction width. As mentioned before, the spin curvature around the constriction is the main source of the measured DWR since the narrowest region contributes most to the resistance. Fig. 2(c) presents the dependence of the spin curvature on constriction width. The smaller the constriction width, the larger the spin curvature and the larger the DWR. When the constriction width decreases from 200 nm to 30 nm, the electron transport occurs from a completely diffusive regime to a quasi-ballistic regime. According to eqn (2) and (3), in both cases, the MR is proportional to  $\lambda^{-2}$ . Our experiment shows that the domain wall-induced MR depends on the constriction width  $d$  through  $d^{-1.87 \pm 0.32}$ , which is consistent with the theory.

According to the power law with the exponent of  $-1.87 \pm 0.32$ , if the cross-sectional area of the CrO<sub>2</sub> nanostructure is reduced to 150 nm<sup>2</sup>, e.g., in a 10 nm-thick film with a 15 nm wide constriction, the corresponding MR would reach approximately 100%. Besides, the simulation shows that when the thin film decreases, the domain wall would be more localized at the nano-constriction, which indicates that even a higher MR could possibly be achieved. In comparison, Lepadatu *et al.* predicted that the MR would be enhanced to about 70% in Ni and 30% in NiFe when the cross-sectional area is reduced to 1 nm<sup>2</sup> which is so small to be practical in fabrication.<sup>14</sup> The cross-sectional area of 150 nm<sup>2</sup> is much more feasible and the predicted large MR of 100% in a simple nanostructure of CrO<sub>2</sub> is a testament to the enhanced magnetotransport of half metals. The DW confined by the geometry can be taken advantage of as an element for applications in magnetic sensing and information storage devices.

## Conclusion

In conclusion, we have investigated the excess resistance induced by a single magnetic DW in a one-dimensional half-metallic CrO<sub>2</sub> nanoscale conductor with a built-in constriction with a variable channel width ranging from 30 to 200 nm. The purpose of the constriction is to localize the magnetic DW in its vicinity, so that an external magnetic field can be applied to generate and annihilate the single magnetic DW. We have uncovered a large size effect of the DWR ratio on the constriction width  $d$ ,  $\frac{\Delta R}{R_0} \propto d^{-1.87 \pm 0.32}$ . We speculate that the large enhancement in DW-induced MR when the constriction width

decreases from 200 nm to 30 nm originates from both DWR and BMR effects. On the one hand, the spin curvature at the constriction increases with decreasing constriction width, and the corresponding DWR increases as in eqn (2). On the other hand, when the constriction width is decreased to 30 nm, the electron transport around the constriction occurs from a diffusive regime to a quasi-ballistic regime. The BMR effect makes an extra contribution to the resistance change. According to the power law derived, we predict that the MR ratio of a simple CrO<sub>2</sub> nanowire impregnated with a constriction at a 150 nm<sup>2</sup> cross-section could reach 100%. This large MR far exceeds that of a conventional ferromagnetic nanowire, confirming the role of half metallicity on enhanced magnetotransport. Based on this study, we conclude that the most effective method to increase the DW-induced MR is to reduce the constriction size, so that the DW is localized as close as possible to the constriction. Our study suggests that magnetic domain structures are active electron transport agents and can be used to design highly functional half-metallic spintronic devices with enhanced performance.

## Conflicts of interest

There are no conflicts to declare.

## Acknowledgements

This work was supported by the National Science Foundation (NSF) under Grant No. OMA-1936221.

## References

- 1 P. M. Levy and S. Zhang, *Phys. Rev. Lett.*, 1997, **79**, 5110.
- 2 L. Qian, W. Chen and G. Xiao, *Nanoscale*, 2020, **12**, 3958–3964.
- 3 U. Ebels, A. Radulescu, Y. Henry, L. Piroux and K. Ounadjela, *Phys. Rev. Lett.*, 2000, **84**, 983.
- 4 D. Buntinx, S. Brems, A. Volodin, K. Temst and C. Van Haesendonck, *Phys. Rev. Lett.*, 2005, **94**, 017204.
- 5 G. Taylor, A. Isin and R. Coleman, *Phys. Rev.*, 1968, **165**, 621.
- 6 J. Gregg, W. Allen, K. Ounadjela, M. Viret, M. Hehn, S. Thompson and J. Coey, *Phys. Rev. Lett.*, 1996, **77**, 1580.
- 7 S. S. Parkin, M. Hayashi and L. Thomas, *Science*, 2008, **320**, 190–194.
- 8 D. A. Allwood, G. Xiong, C. Faulkner, D. Atkinson, D. Petit and R. Cowburn, *Science*, 2005, **309**, 1688–1692.
- 9 Y. Ji, G. Strijkers, F. Yang, C. Chien, J. Byers, A. Anguelouch, G. Xiao and A. Gupta, *Phys. Rev. Lett.*, 2001, **86**, 5585.
- 10 K. Schwarz, *J. Phys. F: Met. Phys.*, 1986, **16**, L211.
- 11 L. Chioncel, H. Allmaier, E. Arrigoni, A. Yamasaki, M. Daghofer, M. Katsnelson and A. Lichtenstein, *Phys. Rev. B: Condens. Matter Mater. Phys.*, 2007, **75**, 140406.

- 12 J. Parker, S. Watts, P. Ivanov and P. Xiong, *Phys. Rev. Lett.*, 2002, **88**, 196601.
- 13 W. Chen, L. Qian and G. Xiao, *Physical Review B*, 2018, **98**, 174402.
- 14 S. Lepadatu and Y. Xu, *Phys. Rev. Lett.*, 2004, **92**, 127201.
- 15 A. Vansteenkiste, J. Leliaert, M. Dvornik, F. Garcia-Sanchez and B. Van Waeyenberge, CAS Article.
- 16 G. Miao, G. Xiao and A. Gupta, *Phys. Rev. B: Condens. Matter Mater. Phys.*, 2005, **71**, 094418.
- 17 A. Biehler, M. Kläui, M. Fonin, C. König, G. Güntherodt and U. Rüdiger, *Phys. Rev. B: Condens. Matter Mater. Phys.*, 2007, **75**, 184427.
- 18 P. Lubitz, M. Rubinstein, M. Osofsky, B. Nadgorny, R. Soulen, K. Bussmann and A. Gupta, *J. Appl. Phys.*, 2001, **89**, 6695–6697.
- 19 S. P. Lewis, P. B. Allen and T. Sasaki, *Phys. Rev. B: Condens. Matter Mater. Phys.*, 1997, **55**, 10253.
- 20 M. Rabe, J. Pommer, K. Samm, B. Özyilmaz, C. König, M. Fraune, U. Rüdiger, G. Güntherodt, S. Senz and D. Hesse, *J. Phys.: Condens. Matter*, 2001, **14**, 7.
- 21 G. Tataru and H. Fukuyama, *J. Phys. Soc. Jpn.*, 1994, **63**, 2538–2562.
- 22 G. Tataru, Y.-W. Zhao, M. Munoz and N. Garcia, *Phys. Rev. Lett.*, 1999, **83**, 2030.
- 23 G. Cabrera and L. Falicov, *Phys. Status Solidi B*, 1974, **61**, 539–549.
- 24 J. B. van Hoof, K. M. Schep, A. Brataas, G. E. Bauer and P. J. Kelly, *Phys. Rev. B: Condens. Matter Mater. Phys.*, 1999, **59**, 138.
- 25 S. Chung, M. Munoz, N. Garcia, W. Egelhoff and R. Gomez, *Phys. Rev. Lett.*, 2002, **89**, 287203.